# Numerical Solving of Dynamic Thermography Inverse Problem for Skin Cancer Diagnosis Based on non-Fourier Bioheat Model

Ivan Dominik Horvat − Jurij Iljaž ⊠ University of Maribor, Faculty of Mechanical Engineering, Slovenia ⊠ jurij.iljaz@um.si

Abstract This paper presents numerical solving of the inverse bioheat problem to estimate four skin cancer parameters; diameter, thickness, blood perfusion rate and thermal relaxation time, based on the thermal response on the skin surface obtained by dynamic thermography and numerical skin cancer model, which can greatly enhance dynamic thermography diagnostics. To describe the heat transfer inside biological tissue and thermal behavior during the dynamic thermography process as realistic as possible, the non-Fourier dual-phase-lag bioheat model was used, as well as skin cancer model has been composed of multilayered healthy skin, embedded skin tumor and subcutaneous fat and muscle. Boundary element method has been used to solve a complex non-Fourier bioheat model to simulate dynamic thermography based on the skin cancer model and guessed searched parameters to obtain the thermal response on the skin surface during the cooling and rewarming phase using a cold air jet provocation, which is needed for the solution of the inverse bioheat problem. The inverse problem has been solved by optimization approach using the hybrid Levenberg-Marquardt optimization method, while the measurement data has been generated numerically with known exact tumor parameters and added noise, to evaluate the accuracy and sensitivity of the solution. Inverse problem solution has been tested for two different thermal responses; absolute temperature and temperature difference response, as well as for two different tumor stages; early stage or Clark II and later stage or Clark IV tumor. All important tumor parameters were successfully retrieved, especially the diameter and relaxation time, even for the high level of noise, while the accuracy of obtained parameters is slightly better using absolute temperature response. The results demonstrate the robustness of the method and a promising way for early diagnosis. The findings contribute to improving bioheat modeling in biological tissues, solving inverse bioheat problems and advancing dynami

**Key words** numerical modeling, dynamic thermography, inverse problem, non-Fourier bioheat transfer, dual-phase-lag model, boundary element method, Levenberg-Marquardt optimization

### **Highlights**

- Non-Fourier dual-phase-lag model improves the heat transfer simulation in skin cancer.
- Dynamic thermography with cold air jet detects tumors during cooling and rewarming.
- Levenberg-Marquardt algorithm estimates tumor diameter, thickness, perfusion rate, and relaxation time.
- Tumor parameters are estimated robustly even with high noise in thermography temperature data.

## 1 INTRODUCTION

In recent years due to the development of infrared (IR) cameras, thermography has become an invaluable tool in science and engineering for many heat transfer problems and applications where measuring or monitoring of the temperature is important. IR camera detects thermal radiation emitted from the observed object, which is then converted into electrical signals to produce thermal images or thermograms. The advantage of this technique is that it measures or records the temperature in a contactless manner for the observed object compared to a thermocouple, which must be in direct contact and measures only at one point [1-3]. Of course, the disadvantage of it is that it can only measure the temperature at the surface and you have to accurately define various parameters like the emissivity of the surface, surrounding temperature, relative humidity etc. to measure surface temperature accurately in an absolute manner. However, the obtained thermal image can still be used in the relative manner, meaning that thermography is mostly used and effective to detect temperature changes based on the recorded temperature contrast of the object surface for various scientific and industrial applications [2,4-7]. For its advantage of recording thermal contrast image in noninvasive manner and the ability to screen larger areas it also found its way in various medical application from diagnostic of breast

cancer, gynecology, kidney transplantation, heart treatment, fever screening, brain imaging, dentistry, cryotherapy, forensic medicine, laser treatments, burn diagnostics to dermatology [8-17].

Medical IR thermography is based on the principle of bioheat transfer govern by blood perfusion, metabolic activity, tissue conductivity and heat exchange with the environment. Therefore, a physiological or pathological change of the tissue is reflected in the change of the tissue temperature or thermal contrast on its surface that can be easily observed with the IR camera. Therefore, the deviation of the surface temperature can signal inflammation, infection, neurological, vascular or metabolic dysfunction and even malignancy due to the higher blood perfusion rate compared to the surrounding healthy tissue [2,8,18-20]. Thermography is especially effective in detecting lesions near tissue surface, like skin cancer. Skin cancer cells differ from normal cells by growing larger due to their rapid and uncontrolled division. This fast-paced growth requires more energy to maintain cellular functions, a process referred to as metabolism. To meet this increased energy demand, the body initiates angiogenesis, where new blood vessels form from existing ones. Melanoma lesions are, therefore, warmer than the surrounding healthy skin, a key indicator used in diagnostic [21-24]. Because medical IR thermography can identify small temperature differences,

DOI: 10.5545/sv-jme.2025.1368 **271** 

it can also detect the growth of new blood vessels or metabolic changes associated with tumor development meaning it can also be a valuable tool for drug or treatment evaluation [25]. The most dangerous form of skin cancer is melanoma that can easily spread to other soft tissues, for which is fatal and responsible for about 75 % of all skin cancer-related deaths [18]. According to Clark et al. [26] and Breslow [27], there is a direct correlation between the survival rate and invasiveness or depth of the melanoma. Clark classified melanoma into five levels from I to V, which is still used nowadays. Clark I and II represent an early stage with more than 72.2 % survival rate, for which an early detection or diagnostic is very important factor to improve the survival in patients with malignant melanoma [26].

Currently, the detection of melanoma mainly relies on a subjective asymmetry, border, color, diameter, evolution (ABCDE) test [28] performed visually by dermatologists, general practitioners or primary care physicians. The ABCDE test provides a qualitative guideline, and it requires a trained specialist to distinguish malignant lesions from benign nevi. Moreover, the ABCDE approach has a relatively high false-alarm probability and moderate detection probability [29]. Since a false negative can lead to metastasis and death, excisional biopsies are routinely performed even on lesions that are non-cancerous [30]. For these reasons, medical IR thermography, especially dynamic thermography, is an emerging promising new technique offering a fast, painless, non-invasive and radiation-free method for early skin cancer diagnosis with high sensitivity and specificity that can achieve rates of up to 99 % [2,18,31].

Medical IR thermography can be done in two ways, first as a static or passive and secondly as dynamic or active thermography. Static thermography obtains the thermal contrast image or thermograms of the skin or tissue under the steady-state condition, while dynamic thermography uses thermal stimulus of the tissue by controlled cooling or heating and observing thermal response of the tissue during the recovery period [17-19,31-34]. Static thermography relies on the natural temperature difference between a tissue and its surroundings, with focus on detection of abnormal temperature variations, which may indicate underlying health concerns. Despite being the most used measurement strategy, it is in certain ways limited. Factors such as bone structure, distribution of blood vessels, recent food or beverage intake, patient positioning, time of day and hormonal cycles can all affect accuracy of this measurement strategy [17,31,35,36]. Feasibility in routine medical practice is further reduced by strict measurement protocols that have been proposed and the need for temperature-controlled rooms where the patient has to acclimatize [17,37]. On the other hand, dynamic thermography can provide quantitative data about investigated tissue, by transient behavior of the tissue due to the thermal stimulus and increased thermal contrast due to the changed rate of bioheat transfer during recovery phase. There are also various ways of stimulating the observed tissue, some of them using conductive heat transfer, electromagnetic radiation or convective heat transfer [17,31]. The most common used thermal stimulus is cooling the tissue with cold gel packs or cold metal disk [19,38-40], and convection cooling using cold air jets [18,33,41]. Research shows that dynamic thermography has multiple advantages over static one. First, the temperature contrast during the recovery phase is increased, making the diagnostic process more accurate, as well as more information about the tissue properties or deep lesion can be retrieved. Secondly, there is no need for the patient to acclimatize or to have a special temperature-controlled room, making the examination period much shorter [17-19,29,31].

Focusing on skin cancer or skin disease diagnosis, medical IR thermography can reach its full diagnostic value potential when paired with accurate bioheat modeling to solve direct and inverse problems

[20,42-45]. Strakowska et al. [19,20] uses simplified one-dimensional (1D) multilayered skin model to evaluate blood perfusion rate and thermal parameters of the skin tissue based on the temperature response of active thermography. Luna et al. [46] used a simple 2D numerical model composed of tumor and healthy surrounding skin to identify thickness and blood perfusion rate of the tumor based on the static thermography information. Similar model has been used by Partridge and Wrobel [47,48] to estimate blood perfusion parameters of the skin tumor, size and position using steady-state skin temperature profile, as well as, Fu et al. [49] to estimate the size and position of the circular tumor or multiple tumors using meshless generalized finite difference method combined with a hybrid optimization algorithm. Bhowmik and Repaka [42] upgraded the skin cancer model to 3D multilayered one to estimate tumor diameter, thickness, blood perfusion rate and metabolic heat generation. Bhowmink et al. [50] also included thermally significant blood vessels into their 3D multilayered skin tumor model to evaluate the effect of blood vessels on finding the position and size of the tumor. Cheng and Herman [43] used simplified 2D multilayered skin tumor model to investigate numerically what type of cooling approach would give the highest temperature contrast between the skin tumor and healthy skin during the recovery phase of dynamic thermography. Cetingül and Herman [33,44] used a more realistic 3D multilayered skin lesion model to evaluate model parameter and tumor shape sensitivity on dynamic thermography temperature contrast. Similar model has also been used by Bonmarin and Gal [51] on investigating lock-in dynamic thermography for detection of early-stage melanoma, as well as Iljaž et al. [52] to solve inverse bioheat problem to evaluate tumor size, blood perfusion rate and metabolic heat generation based on dynamic thermography thermal contrast. Later they improve the skin tumor model by including thermoregulation of the blood perfusion rate to simulate dynamic thermography [53] and solve inverse bioheat problem to evaluate several tumor parameters [45]. All the mentioned models to supplement dynamic or static thermography are based on the Pennes bioheat model that has significant limitations, including the assumption of uniform blood perfusion, the neglect of blood flow direction and countercurrent heat exchange, and the treatment of arterial blood as a constant value [54]. A major drawback of the Pennes model is the assumption of infinite heat propagation speed, which disregards thermal lag effects that become critical in conditions with large heat fluxes in a relatively short period of time especially in inhomogeneous biological structures [55-59]. In those scenarios, Fourier-based bioheat models generally tend to fail in fully capturing the process of heat propagation.

To address the limitations of traditional bioheat transfer models, non-Fourier models have been developed to account for thermal lag and microscale heat transfer effects. Maybe the most important non-Fourier bioheat model is the dual-phase-lag (DPL) model [60,61] introducing a relaxation time for heat flux and temperature gradient and has been used in many bioheat transfer applications, like laser irradiation during hyperthermia treatment, brain tissue heating during laser ablation and nano-cryosurgery [62-64]. DPL model can describe more complex bioheat transfer considering many effects that classical Pennes model cannot describe, however, it has not been used so extensively due to the hyperbolic behavior of the model and its complexity to solve it numerically, as well as unknown tissue relaxation times. The most important research has been done by Liu and Chen [65] investigated the DPL model in a bi-layer spherical tissue domain, using experimental data to estimate relaxation times and demonstrating that the DPL model better captures non-Fourier thermal behavior compared to classical bioheat transfer models, particularly in scenarios involving rapid thermal processes and finite thermal wave propagation. Similar Zhang et al. [66] used

the DPL model to study non-Fourier heat conduction in biological tissues during pulsed laser irradiation. Kishore and Kumar [67] tried to estimate thermal relaxation parameters numerically in laser-irradiated living tissue. All these papers still use very simple tissue models, usually composed out of single or double layer as 1D or 3D axisymmetric problem and constant thermal relaxation parameters.

The literature review highlights that most existing thermography-based skin cancer models rely on the classical Pennes bioheat equation, which assumes uniform perfusion, constant arterial conditions, and infinite heat propagation speed. Such assumptions neglect tissue heterogeneity, blood flow direction, and thermal lag, leading to limitations when modeling rapid transient processes in multilayered biological tissues. Although the non-Fourier dual-phase-lag bioheat model has been introduced in other biomedical contexts, it has not been extensively applied to skin cancer thermography, particularly for inverse problem formulations and the estimation of multiple tumor parameters in realistic geometries.

In this study, these gaps are addressed by applying a non-Fourier dual-phase-lag bioheat model in an axisymmetric multilayered skin tumor domain and formulating the inverse problem using a boundary element method solver combined with a Levenberg–Marquardt optimization approach. The paper is organized as follows: Section 2 introduces the model geometry, governing equations, boundary conditions, and numerical implementation, as well as describes the inverse problem formulation and optimization framework. Section 3 presents the results and discussion, and Section 4 concludes the work with key findings. Overall, this work contributes to the field of mechanical engineering by advancing thermal modeling of heterogeneous biological tissues and providing a more rigorous framework for non-invasive diagnostics using dynamic thermography.

## 2 METHODS AND MATERIALS

### 2.1 Skin Cancer Model

An axisymmetric multilayered numerical model of skin cancer is developed based on our previous work [45,53,68], work of Çetingül and Herman [44], Cheng and Herman [43] and Bhowmik and Repaka [42]. The novelty here is that the model uses non-Fourier DPL bioheat governing equation proposed by Tzou in 1990 [60] making it more general and adapted to the complex bioheat behavior, tissue non-homogeneity and other effects by adjusting the relaxation time parameter. The model presented here is used for dynamic thermography simulation by getting the tumor thermal response.

The most common thermal stimulus for dynamic thermography is cooling the tissue by applying cold gel packs, metal blocks, water immersion, alcohol sprays and even Peltier devices to control the cooling temperature [17,19,38,39,69,70]. The disadvantage of these cooling techniques is that we cannot monitor or record the thermal contrast or response during the cooling period, which can give us additional information about the investigated tissue [68]. Therefore, in this paper we are proposing to use convective cooling approach by temperature adjustable airflow like Ranque-Hilsch vortex tube [18,41]. This way, we can monitor thermal response of the tissue during the cooling and rewarming period of dynamic thermography revealing more information about the investigated tissue, which is needed for successful solving of the inverse problem.

## 2.1.1 Geometry

Skin cancer model is composed of six distinct layers, each with its own thermophysical properties; epidermis, papillary dermis and reticular dermis representing the skin, subcutaneous fat, muscle and tumor, making model more realistic. Çetingül and Herman [44] concluded that the shape of the tumor has little effect on the temperature response on the skin surface during the rewarming period and that most important parameters are average volume and thickness. Therefore, the tumor is represented by cylindrical shape where diameter and thickness represent its effective values. The surrounding healthy tissue has also been modeled with cylindrical shape with the lesion in the center, as can be seen from Fig. 1 showing the whole computational domain of the model. Because of the cylindrical geometry of the domain and skin tumor, as well as adiabatic boundary conditions at the side, the bioheat problem has been treated as an axisymmetric one. This reduces the computational cost due to the computational mesh dimension reduction, which is very important for inverse problem solving. Discretization of an axisymmetric computational domain needed for the numerical simulation, is therefore done with only 2D cross sectional discretization along the rotational axis, as shown in Fig. 2. This drastically reduces the number of computational elements and nodes, speeding up the computational time.

The dimension of the tumor for Clark II and Clark IV has been chosen based on our previous work [45,52,68] and for both examples are gathered in Table 1 together with the layer thicknesses that have been taken from [42-45,53]. The size of computational domain diameter D has been evaluated based on the comparison of temperature contrast from the dynamic thermography simulation, aiming to reduce the effect of adiabatic boundary conditions at the side. The appropriate and chosen domain diameter is D=40 mm, while the height of the skin model is the sum of the heights of all layers and is H=11.6 mm.

## 2.1.2 Non-Fourier DPL Model

In the wave theory of heat conduction, the heat flux and the temperature gradient, are assumed to occur at different times. In 1990, Tzou [60] introduced the DPL model with the aim of eliminating the precedence assumption in the Cattaneo-Vernotte model. It allows either the temperature gradient (cause) to precede the heat flux (effect) or the heat flux (cause) to precede the temperature gradient (effect) in the transient process. This can be mathematically represented by [60]:

$$\mathbf{q}(\mathbf{r}, t + \tau_{a}) = -\lambda \nabla T(\mathbf{r}, t + \tau_{T}), \tag{1}$$

where  $\mathbf{q}$  is the heat flux,  $\mathbf{r}$  an arbitrary space vector, t the physical time,  $\lambda$  the thermal conductivity,  $T = T(\mathbf{r}, t)$  the temperature,  $\nabla$  is the nabla operator,  $\tau_q$  relaxation time of the heat flux and  $\tau_T$  is the relaxation of the temperature gradient. Relaxation time of the heat flux can be also written as  $\tau_q = \omega/C_2$ , where  $\alpha$  is the thermal diffusivity and C the thermal wave speed. For the case of  $\tau_T > \tau_q$ , the temperature gradient established across a material domain is a result of the heat flux, implying that the heat flux vector is the cause and the temperature gradient is the effect. For  $\tau_T < \tau_q$ , heat flux is induced by the temperature gradient established at an earlier time, implying that the temperature gradient is the cause, while the heat flux is the effect.

In a local energy balance, the energy conservation of bioheat transfer is described as [71]:

$$-\nabla \cdot \mathbf{q} + \rho_b w_b c_b (T_b - T) + q_m = \rho c \frac{\partial T}{\partial t}, \tag{2}$$

where  $\rho$  is the tissue density, c the specific heat of the tissue,  $\rho_b$  the blood density,  $c_b$  the specific heat of the blood,  $w_b$  the blood perfusion rate,  $q_m$  the metabolic heat generation and  $T_b$  the arterial blood temperature. The first term on the left-hand side represents heat conduction or diffusion, second term the heat exchange between blood and tissue due to blood perfusion that acts like temperature dependent heat source, the third term the heat generation due to

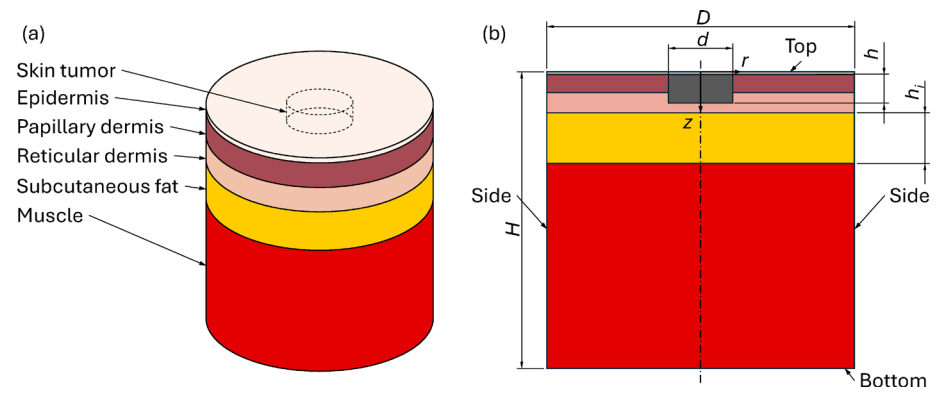


Fig. 1. Computational domain of the axisymmetric multilayered skin tumor model; a) isometric view with named tissues and b) cross sectional view with dimensions and boundary names

the metabolic activity and the term on the right-hand side the heat accumulation. The heat exchange between the arterial blood flow and the tissue proposed Pennes in 1948 [72] who assumed that it happens on the capillary level due to the large interface area. Therefore, the blood perfusion rate represents the volumetric blood flow rate through the capillary network and small arterioles per tissue volume and is non-directional.

Applying first-order Taylor series expansion of the Eq. (1), while neglecting higher-order terms, we can rewrite the definition of the heat flux as:

$$\mathbf{q}(\mathbf{r},t) + \tau_{q} \frac{\partial \mathbf{q}}{\partial t}(\mathbf{r},t) = -\lambda \left\{ \nabla T(\mathbf{r},t) + \tau_{T} \frac{\partial \nabla T(\mathbf{r},t)}{\partial t} \right\}. \tag{3}$$

Implementing Eq. (3) to the Eq. (2) yields the (type I) DPL equation of bioheat transfer [61,68]:

$$\tau_{q}\rho c \frac{\partial^{2}T}{\partial t^{2}} + \left(\rho c + \tau_{q} w_{b} \rho_{b} c_{b}\right) \frac{\partial T}{\partial t} = 
= \lambda \nabla^{2}T + \tau_{T} \lambda \frac{\partial \nabla^{2}T}{\partial t} + w_{b} \rho_{b} c_{b} (T_{b} - T) + q_{m}, \tag{4}$$

where heat conductivity of the tissue and metabolic heat generation assumed to be constant;  $\lambda = \text{const.}$  and  $q_m = \text{const.}$  The first term on the left-hand side of the Eq. (4) represents the hyperbolic term that captures thermal inertia due to the finite speed of heat propagation, which is otherwise not present in the bioheat models using Fourier law of heat conduction. The second term on the left-hand side is the energy storage term from the classical heat conduction, that is now extended to account for the delayed effect of blood perfusion on heat transfer. The first term on the right-hand side represents classical heat conduction, while the second term, which is the mixedderivative term dramatically alters the fundamental characteristics of heat propagation, by removing the wave behavior of the hyperbolic type of equation becoming parabolic in its nature. In the case of  $\tau_a$ =0 and  $\tau_T$ =0 or  $\tau_a$ = $\tau_T$ , the DPL model reduces to the classical Pennes

The non-Fourier DPL bioheat model given by Eq. (4) is written for each layer or tissue of the skin cancer model, assuming constant material properties and parameters. Equilibrium and compatibility conditions have to be prescribed at the interface between two adjoint tissues to describe the bioheat transfer in the whole computational domain. The compatibility condition at the interface is:

$$T_i(\mathbf{s},t) = T_{i+1}(\mathbf{s},t),\tag{5}$$

where indices i and i+1 represent adjoint layers and s position vector of the interface boundary. This condition represents that there is no contact resistance between the layers. While equilibrium condition represents the conservation of energy and is written as:

$$\mathbf{q}_{i}(\mathbf{s},t)\cdot\mathbf{n}_{i} = \mathbf{q}_{i+1}(\mathbf{s},t)\cdot\mathbf{n}_{i+1},\tag{6}$$

where **n** represents the normal vector. By applying definition of the heat flux given by Eq. (3) to the equilibrium condition, it can be rewritten in the following form:

$$\left[ -\lambda_{i} \left( \nabla T_{i} + \tau_{T,i} \frac{\partial \nabla T_{i}}{\partial t} \right) - \tau_{q,i} \frac{\partial \mathbf{q}_{i}}{\partial t} \right] \cdot \mathbf{n}_{i} =$$

$$\left[ -\lambda_{i+1} \left( \nabla T_{i+1} + \tau_{T,i+1} \frac{\partial \nabla T_{i+1}}{\partial t} \right) - \tau_{q,i+1} \frac{\partial \mathbf{q}_{i+1}}{\partial t} \right] \cdot \mathbf{n}_{i+1}, \tag{7}$$

which is complex and not easy to implement. For the example when  $\tau_{q,i} = \tau_{q,i+1}$  and  $\tau_{T,i} = \tau_{T,i+1}$  the equilibrium condition can be rewritten in the form  $-\lambda_i \nabla T_i \cdot \mathbf{n}_i = -\lambda_{i+1} \nabla T_{i+1} \cdot \mathbf{n}_{i+1}$  which is well known equilibrium condition in heat transfer.

## 2.1.3 Boundary Conditions

Because the bioheat problem has been treated as axisymmetrical, the tissue temperature and other field functions like heat flux has been transformed from classical cartesian coordinate system to cylindrical one which does not depend on the angle;  $T(x,y,z,t) \rightarrow T(r,z,t)$ , and where r represents the radial distance from the center and z the depth from the top of domain.

To simulate dynamic thermography, it is essential to define appropriate initial and boundary conditions for the computational domain. For the bottom section of the domain, Dirichlet boundary condition is applied. This choice is based on the assumption that the muscle tissue is thick enough to preserve body core temperature throughout both the cooling and warm-up phases. Therefore, at the bottom we prescribed the following condition:

$$T(r,z,t) = T_{bc}, \quad z = H, \quad 0 \le r \le D/2, \quad 0 \le t \le t_{sim},$$
 (8)

where  $T_{bc}$  is the body core temperature and  $t_{sim} = t_{cool} + t_{warm}$  is the total simulation time, which is composed of the cooling time  $t_{cool}$ , and the warm-up time  $t_{warm}$ . The body core temperature can vary between 36.5 °C to 37.5 °C and has chosen to be  $T_{bc}$ =37 °C, as this is considered to be the average core body temperature of a healthy person at rest [17,44,52].

On the sides of the domain we prescribed adiabatic boundary condition, based on the assumption that there are no side effects that will influence the thermal contrast of the lesion:

$$\mathbf{q}(r,z,t) = 0 \rightarrow \frac{\partial T}{\partial r}(r,z,t) = 0, \ 0 \le z \le H, \ r = D / 2, \ 0 \le t \le t_{sim}, \ (9)$$
  
To simulate cooling with the cold air jet and rewarming period, we

prescribed Robin boundary condition as:

$$\mathbf{q}(r,z,t) = \frac{\partial T}{\partial r}(r,z,t) = \alpha \left(T(r,z,t) - T_{\infty}\right),$$

$$z = 0, \quad 0 \le r \le D/2, \quad 0 \le t \le t_{\text{vim}}, \tag{10}$$

where  $\alpha$  represents the heat transfer coefficient of the cooling air jet during the cooling time or the heat transfer coefficient to the environment during the rewarming time, and  $T_{\infty}$  denotes the temperature of the cooling jet or ambient temperature. During the cooling phase, the heat transfer coefficient was set to  $\alpha$ =50 W/(m²K) and the temperature of the cold air jet to  $T_{\infty}$ =5 °C. After cooling time  $t_{cool}$ , the cold air jet is removed, and rewarming occurs due to metabolic heat production, blood perfusion and heating from the environment. In the rewarming phase, the heat transfer coefficient is reduced to  $\alpha$ =10 W/(m²K), and the ambient temperature is set to  $T_{\infty}$ =22.4 °C which is the same condition used for the steady-state simulation and is based on the following work [33,45,52,68].

The total simulation time has been set to  $t_{sim}$ =80 s, with the cooling phase lasting  $t_{cool}$ =30 s and the rewarming phase  $t_{warm}$ =50 s. The choice of a 30 s cooling phase is based on the work of Godoy et al. [73] that used a rewarming duration of  $t_{warm}$ =120 s. We deliberately opted for relatively short cooling and rewarming times compared to other studies [42,52], as our primary focus is to examine the thermal behavior of tissue under highly transient conditions, and to shorten the examination period of the dynamic thermography.

The initial temperature condition T(r,z,t=0) was set to the steady-state solution of the bioheat problem, determined by the boundary conditions specified with Eq. (8) to Eq. (10). This approach assumes that the patient has already acclimated to the conditions in the examination room.

# 2.1.4 Model Parameters

Material properties for each tissue layer can vary a lot and are not determined exactly as stated by Çetingül and Herman [44]. Therefore, the material properties have been taken as an average value found in the literature and can also be found in the work of other authors [33,42-45,52]. For tumor with different stages, we assumed and prescribed the same material properties, due to the lack of more precise data; therefore, stage differs only with the size of the tumor as suggested by Clark [26]. Table 1 gathers the material properties like density, specific heat, blood perfusion rate, relaxation times etc., used in the presented skin tumor model together with the tissue dimensions.

Relaxation times  $\tau_q$  and  $\tau_T$  needed for the non-Fourier DPL bioheat model remains challenging to define exactly due to the lack of experimental data, significant variability and ongoing debate. For processed meat, these values are estimated to be  $\tau_q$ =14 s to 16 s and  $\tau_T$ =0.043 s to 0.056 s, while for muscle tissue from cow have shown values  $\tau_g$ =7.36 s to 8.43 s and  $\tau_T$ =14.54 s to 21.03 s [65,74]. The relaxation times  $\tau_q$  and  $\tau_T$  in this work were determined based on the expressions provided in the generalized DPL model by Namakshenas et al. [59] that is based on the tissue porosity as well. However, in this work the influence of porosity is taken into account through effective tissue properties instead. The relaxation times  $\tau_q$  and  $\tau_T$  can be estimated using the following expressions [59]:

$$\tau_{q} = \frac{\varepsilon(1-\varepsilon)}{\left[\frac{\varepsilon}{c_{tb}} + (1-\varepsilon)\right]} \frac{\rho_{b}c_{b}}{G},$$
(11)

$$\tau_{T} = \frac{\varepsilon (1 - \varepsilon)}{\left[\frac{\varepsilon}{\lambda_{tb}} + (1 - \varepsilon)\right]} \frac{\rho_{b} c_{b}}{G},$$
(12)

where  $c_{tb} = \rho c/\rho_b c_b$  represents the stored energy of the tissue relative to that of the blood, while  $\lambda_{tb} = \lambda/\lambda_b$  denotes the thermal conductivity of the tissue compared to the blood. G is the coupling factor between the tissue and blood, defined as [59]:

$$G = \frac{4\varepsilon \lambda_b}{d_b^2} Nu + \rho_b w_b c_b,$$
(13)

where Nu is the Nusselt number and  $d_b$  the representative artery diameter of the tissue.

The thermal relaxation time  $\tau_q$  for all layers, except the tumor and epidermis, was determined based on Eq. (11) by prescribing Nusselt number to Nu=4.93 and artery diameter to  $d_b=1.5$  mm, representing average value for the skin and muscle.

For tumor layer we assigned a higher  $\tau_q$  value than the other tissues to reflect its increased perfusion rate and structural inhomogeneity [75], therefore, we set it to  $\tau_q$ =3.0 s for the tumor. In contrast, the epidermis, which lacks blood vessels and is more uniform than other tissue layers, was given a lower thermal relaxation time. We set  $\tau_q$  for the epidermis to  $\tau_q$ =0.3 s, assuming that despite its homogeneity, it still introduces some thermal resistance due to delayed heat transfer. The values for  $\tau_T$  were selected based on the stability criteria for DPL presented by Quintanilla and Racke [76]. In this study,  $\tau_T$  was chosen to be half of  $\tau_q$ , with  $\tau_T/\tau_q$ =1/2, in order to satisfy the stability limits commonly associated with higher-order Taylor series expansions. The values chosen for the  $\tau_q$  and  $\tau_T$  for each tissue are also gathered in Table 1.

The arterial blood temperature needed for governing equation is assumed to be as equal as defined body core temperature;  $T_b = T_{bc} = 37.0$  °C.

### 2.1.5 Solver and Discretization

Presented multilayered skin cancer model based on the non-Fourier DPL bioheat equation to simulate dynamic thermography is highly non-linear and numerically difficult to solve. For this reason, we wrote our own solver based on the subdomain BEM approach using elliptic axisymmetric fundamental solution and quadratic elements, which has been tested on bench-mark problems of other authors [77-79]. A detailed description of the solver and numerical discretization of non-Fourier DPL model with the treatment of equilibrium condition at the interface can be found in our previous work [68]. The maximum number of non-linear steps for dynamic thermography simulation and inverse bioheat problem was set to  $l_{max}$ =20, with a maximum error tolerance of  $\varepsilon$ =1·10<sup>-8</sup>.

To discretize computational domain, we used our own 2D structured mesh generator with the representative spatial element size of  $\Delta r = \Delta z = 0.5$  mm, with minimal number of 2 elements in z direction in each layer. A non-uniform mesh was used with an expansion factor of  $\zeta=1.1$  in both spatial directions from the center. The reason for using own mesh generator is due to the inverse problem solving, where diameter and thickness of the tumor is changing during the optimization process where generation of a new mesh must be done. For the Clark II example, the computational mesh consists of 360 computational cells and 1517 computational nodes, while for the Clark IV example the mesh includes 442 computational cells and 1855 nodes and is presented in Fig. 2. The difference in mesh density between these two examples is because of different tumor sizes, generating different element sizes for tumor discretization, which affects the size of the structured mesh for the whole computational domain. Presented mesh density has been confirmed to be adequate following a mesh sensitivity study. Similar, by time step sensitivity analysis, we define the time step needed to describe the transient behavior of the model. For time discretization of  $t_{sim}$  = 80 s a constant time step of  $\Delta t = 0.5$  s has been taken.

Table 1. Tissue dimensions and material properties of the skin cancer model

Layer	<i>d</i> [mm]	h [mm]	ho [kg/m³]	$c_p$ [J/(kg K)]	λ [W/(mK)]	$w_b [s^{-1}]$	$q_m$ [W/m $^3$ ]	$ au_q$ [S]	$ au_T[s]$
Epidermis	-	0.1	1200	3589	0.235	_	_	0.30	0.15
Papillary Dermis	-	0.7	1200	3300	0.445	0.0002	368.1	2.28	1.14
Reticular Dermis	-	8.0	1200	3300	0.445	0.0013	368.1	2.46	1.23
Fat	-	2.0	1000	2674	0.185	0.0001	368.3	2.16	1.08
Muscle	-	8.0	1085	3800	0.510	0.0027	684.2	2.22	1.11
Blood	-	_	1060	3770	_	_	_	-	_
Tumor Clark II	2.0	0.44	1030	3852	0.558	0.0063	3680	3.00	1.50
Tumor Clark IV	2.5	1.1	1030	3852	0.558	0.0063	3680	3.00	1.50

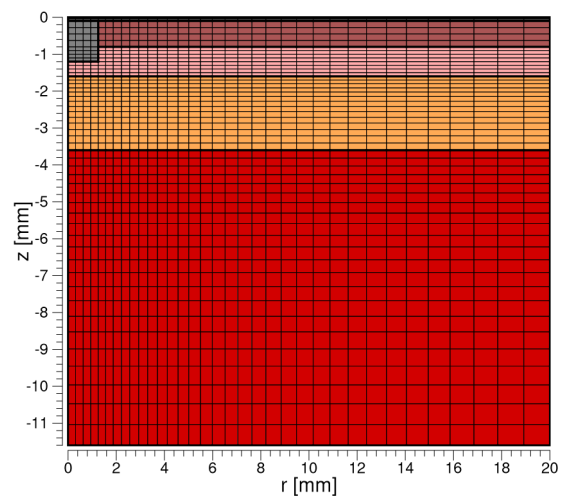


Fig. 2. 2D computational mesh representing axisymmetric cylindrical domain for Clark IV example

## 2.2 Inverse Bioheat Problem

When the numerical simulation of certain processes or phenomena is needed, we are talking about direct problem. For example, the simulation of dynamic thermograph is direct bioheat problem, where we must prescribe governing equation of the process, geometry, all material or model properties and boundary conditions describing the process. These problems are well-posed, meaning that they have a unique and stable solution that can be obtained using established numerical or analytical methods. However, when certain parameters, such as material properties, boundary conditions or internal sources, are unknown and must be estimated from indirect measurements, we encounter what is known as inverse problem. Inverse problems seek to determine unknown inputs based on observed outputs. Their solution depends on the mathematical model used and is often sensitive to measurement noise or model inaccuracies, which can lead to instability or non-uniqueness of the solution, characteristics that make inverse problems ill-posed by nature [42,45-47,52,80,81].

To solve inverse problem an optimization approach has been used. The inverse problem is transformed to optimization process by objective function that measures the difference between simulated temperature response and actual measurement data. The solution of the inverse problem is represented by the minimum of the objective function. A well-posed inverse problem should have only one global minimum; otherwise, the solution is not unique, making parameter estimation unreliable [42,45,52].

This paper covers two test examples; Clark II and Clark IV, to evaluate their important properties based on two different thermal responses of the tissue, first the absolute temperature;  $T_{abs}$ , and second the temperature difference regarding to the healthy skin;

 $\Delta T$ . Therefore, this paper covers four different inverse problems, to evaluate the feasibility of early skin cancer diagnosis and solution sensitivity regarding to type of the recorded thermal image.

#### 2.2.1 Measurement Data

Dynamic thermography measurements have been generated numerically by solving direct bioheat problem with known searched parameters and by adding a measurement noise to simulate more realistic measurement data and not to commit inverse crime.

First test example uses early stage (Clark II) skin tumor with the following searched parameters; d=2.0 mm, h=0.44 mm,  $w_b=0.0063$  s<sup>-1</sup>,  $\tau_q=3.0$  s, and the second one the later stage (Clark IV) tumor with the following searched parameters; d=2.5 mm, h=1.1 mm,  $w_b=0.0063$  s<sup>-1</sup>,  $\tau_q=3.0$  s, that has already been introduced in Section 1 and gathered in Table 1. These parameters are written here again due to clarity, because they represent the exact values of the considered inverse problems.

Thermal response during the dynamic thermography has been recorded in two ways, first as an absolute temperature value and second as the temperature difference. Fig. 3 shows the absolute temperature response of simulated dynamic thermography for Clark II and Clark IV tumor, while Fig. 4 and 5 show the temperature difference response. As can be seen, the temperature contrast or difference between the tumor temperature and surrounding healthy skin is increased during the cooling phase by almost two times, compared to the steady-state conditions. This is the advantage of dynamic thermography. The temperature spatial profile is the same regarding the absolute or temperature difference response, while the transient behavior is different, as can be seen from Fig. 3 and 4. For better understanding, Fig. 5 is simulating the processed IR image at the end of the cooling phase together with the tumor dimension, where enhanced contrast of dynamic thermography is obtained. It can be observed that early-stage tumors produce lower temperature contrast than later-stage ones meaning it can be harder to detect and

Measurement data obtained at the surface of the skin z=0 for position p and time t can be written as:

$$T_{abs,s,p,t} = T(r_p, 0, t_t),$$
 (14)

$$\Delta T_{s,p,t} = T(r_p, 0, t_t) - T(D/2, 0, t_t), \tag{15}$$

where index *s* represents simulation,  $r_p$  the radial position of the measurement points and  $t_t$  the time of the measurement taken. Measurement data resolution is very important for successful parameter estimation, as it needs to describe the temperature response adequately. The measurement points have been taken in the radial range of  $r_p \in [0 \text{ mm}, 5 \text{ mm}]$  at  $n_p = 6$  equally spaced points meaning that the distance between two measurement points is  $\delta_r = 1 \text{ mm}$ . While for the time measurement the data has been taken during cooling, as well as rewarming period of dynamic thermography;  $t_t \in [0 \text{ s}, 80 \text{ s}]$  at intervals of  $\delta_t = 1 \text{ s}$  generating  $n_t = 81$  time measurement

points. We notice that this measurement resolution is fine enough to capture tissue temperature response and to be able to evaluate tumor parameters. Finer resolution did not increase the accuracy of the searched parameters, while coarser resolution, especially in time domain, increased the error in the estimated parameters.

To mimic real measurement data a white noise has been added to the generated measurement data as:

$$T_{abs,m,p,t} = T_{abs,s,p,t} + \eta \Delta T_{err}, \tag{16}$$

$$\Delta T_{m,p,t} = \Delta T_{s,p,t} + \frac{\eta}{2} \Delta T_{err}, \tag{17}$$

where  $\eta$  represents a random number;  $\eta \in [-1, 1]$ , index m stands for measurement data and  $\Delta T_{err}$  the temperature uncertainty level. The second term on the right-hand side represents the temperature deviation or noise. Modern IR cameras can obtain noise equivalent temperature difference (NETD) value of less than 30 mK. Therefore, we investigate test examples under three levels of uncertainty; 0 mK, 25 mK and 50 mK [45,52]. The first one represents exact measurement data, while the last two represent low and high level of noise. In the

last two cases, the measurement data does not follow numerical model anymore and therefore no inverse crime is committed. Because the noisy measurement data are generated randomly, we generated three different measurement sets for each test example and noise level, except for the exact one. This way we can also analyze how the randomness of the added white noise affects the inverse solution.

For a clear presentation Fig. 6 shows the generated measurement data compared to the simulated dynamic thermography response or exact data for Clark II and Clark IV test example. As can be seen, the level of noise can affect the temperature response for the Clark II more than for Clark IV, which makes solving inverse problem more difficult and poor accuracy to be expected for early-stage tumor.

# 2.2.2 Objective Function

Objective function measures the difference between simulated temperature response of dynamic thermography by guessed searched parameters and generated measurement data in our case. Therefore, the objective function for the absolute temperature response can be defined as:

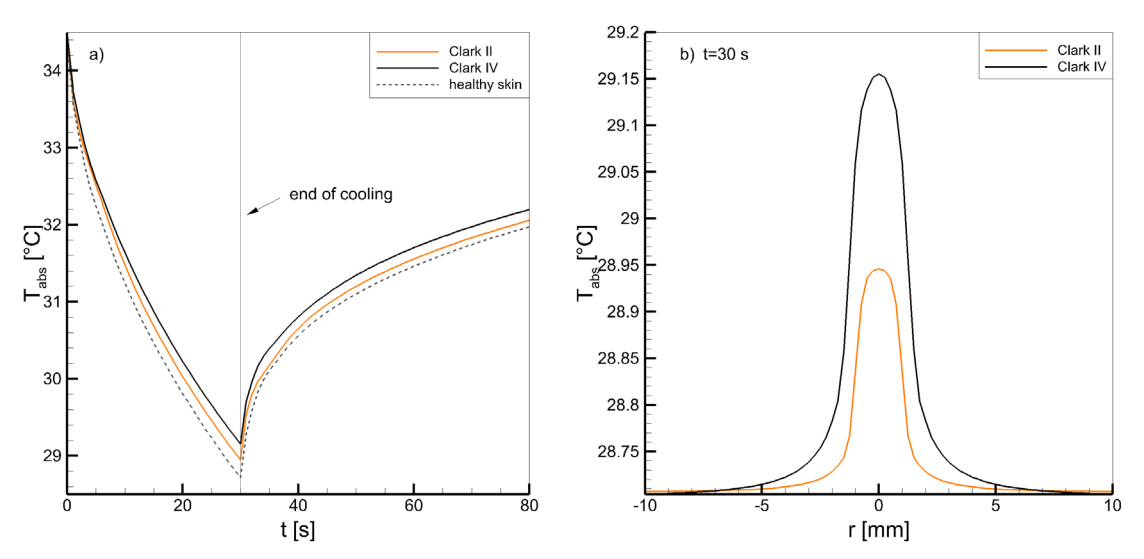


Fig. 3. Simulated absolute temperature response  $T_{abs,s}$  at the skin surface for Clark II and Clark IV tumor during dynamic thermography: a) transient response for tumor position r=0 and healthy skin at position r=D/2, and b) radial temperature distribution at the end of cooling phase t=30 s

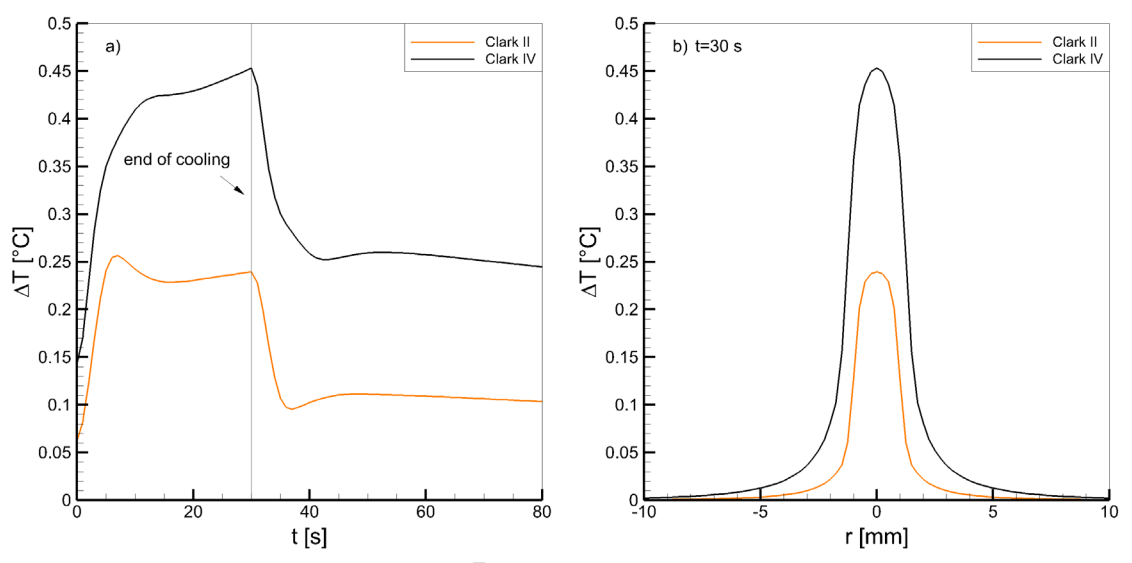


Fig. 4. Simulated temperature difference response  $\Delta T_s$  at the skin surface for Clark II and Clark IV tumor during dynamic thermography: a) transient response of maximal temperature difference measured at the center of the tumor, b) radial temperature difference distribution at the end of cooling phase t = 30 s

$$F_{1}(\mathbf{y}) = \sum_{t=1}^{n_{t}} \sum_{p=1}^{n_{p}} \left( T_{abs,s,p,t}(\mathbf{y}) - T_{abs,m,p,t} \right)^{2}, \tag{18}$$

and for the temperature difference or temperature contrast as:

$$F_2(\mathbf{y}) = \sum_{t=1}^{n_t} \sum_{p=1}^{n_p} \left( \Delta T_{s,p,t}(\mathbf{y}) - \Delta T_{m,p,t} \right)^2, \tag{19}$$

where indices 1 and 2 stand for the absolute and temperature difference thermal response, respectively,  $F(\cdot)$  is the objective function value,  $\mathbf{y}$  is the vector of unknown parameters, indices t and p correspond to the time and location of temperature measurements, while  $n_t$  and  $n_p$  represent the number of observed time points and measurement locations. Vector  $\mathbf{y}$  is defined as  $\mathbf{y} = \{y_j; j=1,...,n\} = \{d,h,w_b,\tau_q\}$ , where n=4 is the number of searched parameters.

## 2.2.3 Levenberg-Marquardt Algorithm

Deterministic optimization methods work faster and require fewer evaluations compared to stochastic methods [49] like particle swarm optimization (PSO) [82], design of experiment (DOE), differential evolution (DE) [83] or simulated annealing (SA), when objective function is smooth and computational cost for direct problem is high.

In this work, the LM optimization algorithm is chosen because it balances the advantages of the steepest descent and Gauss-Newton methods, making it well-suited for nonlinear least-squares problems [45,84].

The optimization problem is formulated as:

find 
$$\mathbf{y}^* = \arg\min_{\mathbf{y}} [F(\mathbf{y})],$$
 (20)  
where  $\mathbf{y}^*$  represents the minimum of the objective function and

where  $y^*$  represents the minimum of the objective function and solution of the inverse problem. The optimization is performed iteratively, updating the unknown parameter values using:

$$\mathbf{y}_{k+1} = \mathbf{y}_k + \beta_{\nu} \mathbf{s}_k \Rightarrow F(\mathbf{y}_{k+1}) < F(\mathbf{y}_k), \tag{21}$$

where **s** represents the search direction,  $\beta$  is the step size, and indices k and v denote iteration and trial step indices, respectively. LM algorithm finds the search direction at each iteration step as the solution to the equation system:

$$\left(\mathbf{J}_{k}^{tr}\cdot\mathbf{J}_{k}+\mu_{k}\mathbf{I}\right)\mathbf{s}_{k}=-\mathbf{J}_{k}^{tr}\cdot\mathbf{f}(\mathbf{y}_{k}),\tag{22}$$

where **J** represents the Jacobian matrix,  $\mu$  is a damping parameter, **I** the identity matrix and  $\mathbf{f}(\cdot)$  represents the residual vector;  $F(\mathbf{y}) = \mathbf{f}^{tr}(\mathbf{y}) \cdot \mathbf{f}(\mathbf{y}) \rightarrow \mathbf{f}(\mathbf{y}) = \{f_i; i=1,...,m\}$ , where  $m = n_i n_p$ . In each iteration step the Jacobian matrix and damping parameter must be

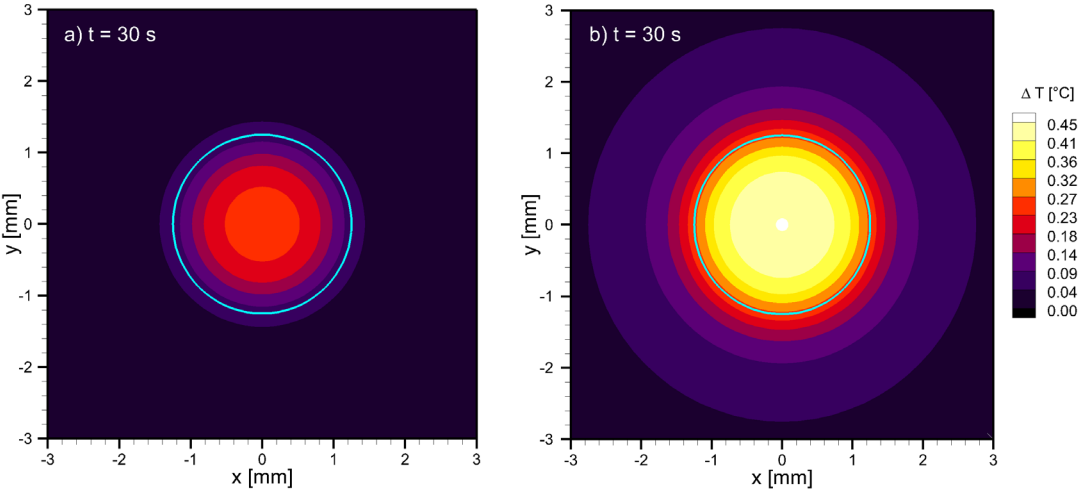


Fig. 5. Simulated temperature difference  $\Delta T_s$  contour at the skin surface, simulating the IR image at the end of the cooling phase for; a) Clark IV and b) Clark IV tumor, while blue line represents tumor diameter

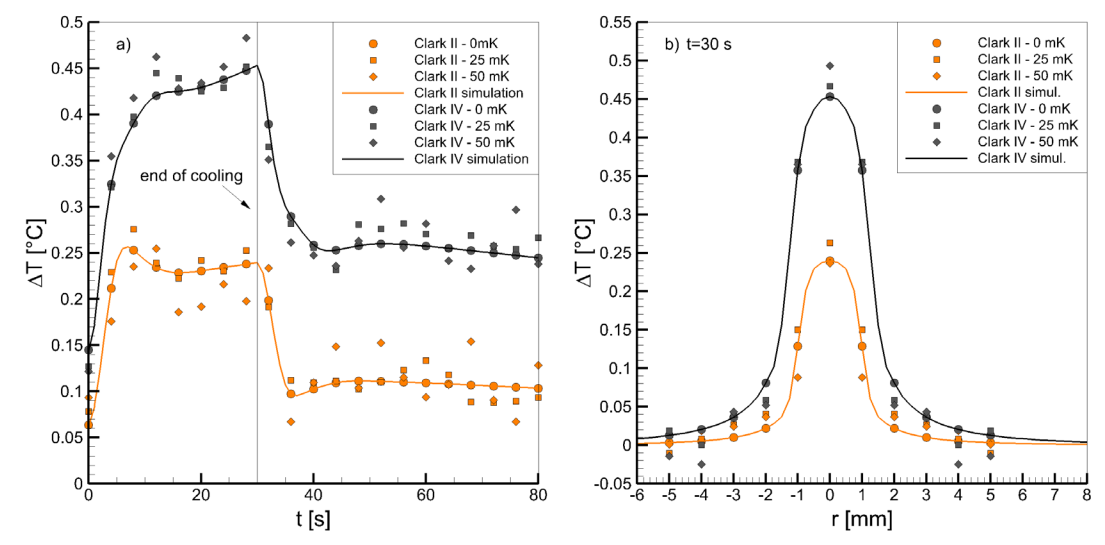


Fig. 6. Representation of numerically generated measurement data of temperature difference response  $\Delta T_m$  for Clark II and Clark IV tumor using 0 mK, 25 mK and 50 mK level of noise: a) transient response at the center of the tumor, and b) radial response at the end of cooling phase t = 30 s

calculated and updated. The Jacobian matrix is evaluated numerically using first-order finite difference scheme as:

$$J_{i,j} = \frac{\partial f_i}{\partial y_j} \approx \frac{f_i(y_j + \Delta y_j) - f_i(y_j)}{\Delta y_j},$$
(23)

where indices i and j represent the row and column of matrix J, and  $\Delta y_j$  represents the change of parameter j, which has been taken as 1 % of its value;  $\Delta y_j = 0.01y_j$ .

Once the search direction  $\mathbf{s}_k$  is known the solution can be updated using Eq. (21) where the descent criteria is checked;  $F(\mathbf{y}_{k+1}) < F(\mathbf{y}_k)$ . The step size is taken as  $\beta_0 = 1$  for the first trial, as the search direction is also controlled by the damping parameter  $\mu$ . If the descent criteria is not met, the step size is then reduced by  $\beta_{\nu+1} = \beta_{\nu}/2$ .

The damping parameter is updated by equation:

$$\mu_{k+1} = \mu_k \max \left[ \frac{1}{3}, 1 - (2\theta_k - 1)^3 \right],$$
 (24)

where  $\theta$  represents the gain ratio as:

$$\theta_k = \frac{F(\mathbf{y}_k) - F(\mathbf{y}_{k+1})}{Z(0) - Z(\beta_k \mathbf{s}_k)},\tag{25}$$

where  $Z(\cdot)$  represents a linear Taylor expansion of the objective function. For the first iteration step, the damping parameter has been chosen to be  $\mu_0 = 10^{-5} \text{max}(\mathbf{J}^{tr} \cdot \mathbf{J})$ .

To stop the optimization algorithm, we used three stopping criteria where only one of them has to be fulfilled:

$$k > k_{max}, \tag{26}$$

$$\left\| \mathbf{J}_{k}^{T} \cdot \mathbf{f} \left( \mathbf{y}_{k} \right)_{x} \right\| \leq \varepsilon_{1}, \tag{27}$$

$$\|\mathbf{y}_{k+1} - \mathbf{y}_k\| \le \varepsilon_2 (\|\mathbf{y}_k\| + \varepsilon_2),$$
 (28)

where  $k_{max}$  represents the maximum number of iterative steps and  $\varepsilon_1$  and  $\varepsilon_2$  the tolerance for the gradient and step size, respectively. The maximum number of iterative steps has been chosen to be  $k_{max} = 50$ , while the tolerance for the second and third criteria has been taken as  $\varepsilon_1 = \varepsilon_2 = 10^{-8}$ .

Table 2. Different starting points for the optimization process

Example	$y_0$	d [mm]	h [mm]	$w_b  [s^{-1}]$	$\tau_q$ [S]
	1	2.3	0.60	0.0080	3.5
Clark II	2	1.9	0.50	0.0060	2.8
	3	1.7	0.30	0.0050	1.5
	1	2.4	0.90	0.0090	3.7
Clark IV	2	2.6	1.20	0.0060	2.8
	3	1.8	0.70	0.0050	1.7

# 2.2.4 Starting Point

To test the stability of the inverse solution depending on the initial guess, we have chosen three different starting point of optimization process. Table 2 is gathering the different initial guesses for the optimization process for Clark II and Clark IV example. One starting point is close to the exact solution, while other two are more off.

## 3 RESULTS AND DISCUSSION

Results of the inverse bioheat problem are presented in tables, which are the most appropriate to show the estimated value of the searched parameters. For better representation of results accuracy, the relative error for certain parameters is highlighted with the gray color in the tables where intensity reflects its level. This section covers the analysis of the starting point, measurement noise and randomness of the measurement data using the absolute temperature response, while at the end the effect of thermal response type is presented.

## 3.1 Starting Point

The analysis of the starting point has been carried out first to evaluate its effect on the solution of the inverse problem and stability of the optimization process. Table 3 shows the solution of the inverse problem together with the relative error regarding the starting point for Clark IV tumor using absolute temperature response. The solution for the exact measurement data; 0 mK, coincidence with the exact data and does not depend on the starting point. Solution of the inverse problem also does not depend strongly on the starting point for the noisy measurement data; however, there can be a slight difference but negligible. The average objective function value reached for the exact measurement data was 1.39·10<sup>-9</sup> K<sup>2</sup> in 12 optimization steps. While for the noisy measurement data the objective function value increased to  $2.65 \cdot 10^{-2} \text{ K}^2$  for the 25 mK noise and to  $1.07 \cdot 10^{-1} \text{ K}^2$ for the 50 mK with the average number of optimization steps 10, because the measurement data does not follow the numerical model exactly due to the noise. Similar observation and conclusion have been made using different set of measurement data, Clark II example and temperature difference response, and is therefore omitted here.

At this point, we can conclude that solution of the inverse bioheat problem using LM algorithm does not depend on the initial guess or starting point making optimization method stable, as well as that convergence of the optimization process is fast.

## 3.2 Measurement Noise and Data

Here, we would like to evaluate how the level of measurement noise and randomness of generating the measurement data set affects

Table 3. Solution of the inverse problem for Clark IV example using different starting points and absolute temperature response;  $F_1(\mathbf{y})$ , together with relative error

			Sol	ution		Relative error			
$\Delta T_{err}$	$\mathcal{Y}_0$	<i>d</i> [mm]	h [mm]	$w_b  [s^{-1}]$	$ au_q$ [S]	d [%]	h [%]	w <sub>b</sub> [%]	$\tau_q$ [%]
	Exact	2.50000	1.10000	0.006300	3.00000				•
	1	2.50002	1.09995	0.006300	3.00002	0.00	0.00	0.01	0.00
0 mK	2	2.50001	1.09996	0.006300	3.00001	0.00	0.00	0.00	0.00
	3	2.50002	1.09996	0.006300	3.00001	0.00	0.00	0.00	0.00
	1	2.50889	1.11174	0.006188	2.97513	0.36	1.07	1.78	0.83
25 mK	2	2.50997	1.09994	0.006230	2.97529	0.40	0.01	1.11	0.82
	3	2.50909	1.11072	0.006191	2.97496	0.36	0.97	1.73	0.83
	1	2.51047	1.00056	0.006691	3.03187	0.42	9.04	6.21	1.0
50 mK	2	2.51011	1.00098	0.006691	3.03156	0.40	9.00	6.21	1.05
	3	2.51019	1.00031	0.006694	3.03156	0.41	9.06	6.25	1.05

Table 4. Solution of the inverse problem for Clark II example using different measurement data set of absolute temperature response;  $F_1(\mathbf{v})$ , together with relative error

			Soli	ution		Relative error			
$\Delta T_{err}$	$\mathcal{Y}_0$	d [mm]	h [mm]	$w_b  [s^{-1}]$	$ au_q$ [S]	d [%]	h [%]	<i>w<sub>b</sub></i> [%]	$\tau_q$ [%]
	Exact	2.00000	0.44000	0.006300	3.00000				·
25 mK	1	2.00000	0.43494	0.006380	2.99436	0.00	1.15	1.26	0.19
	2	2.00000	0.43730	0.006314	2.96224	0.00	0.61	0.22	1.26
	3	2.00000	0.44054	0.006271	3.03409	0.00	0.12	0.46	1.14
50 mK	1	2.01886	0.43046	0.006178	3.03609	0.94	2.17	1.93	1.20
	2	2.00000	0.46098	0.006174	2.91235	0.00	4.77	2.00	2.92
	3	2.00000	0.42768	0.006426	2.95631	0.00	2.80	2.00	1.46

the solution. Because, it has been shown that the solution does not depend on the starting point, we set starting point 3 for all our further calculations. Table 4 shows the obtained results for Clark II example using absolute temperature response and different data sets for 25 mK and 50 mK noise level together with relative error. As can be seen, the solution varies on the randomness of the noise or measurement data set and the relative error of the solution increases by increasing the level of noise. Diameter of the tumor d can be determined very accurately, while other parameters have the same level of error, however, still under 5 %, meaning a good estimation or retrieval of the searched parameters. Similar findings have also been found for Clark IV example and are therefore omitted here.

From this small analysis, we can conclude that the solution of the inverse problem depends on the level of the noise and randomness of the generated measurement data set. Therefore, it is important to generate or record more than one measurement data set to evaluate the deviation of the solution.

Because inverse problem solution depends on the randomness of the measurement data, it is better to use statistical indicators like mean value, deviation and coefficient of variation (COV). We are well aware that three different solutions are too small sample size to make accurate statistical analysis, however, it can still give us the

Table 5. Solution of the inverse bioheat problem for Clark II and Clark IV example under noisy measurement data sets of absolute temperature response;  $F_1(\mathbf{y})$ , showing the mean value, deviation, COV and mean relative error

	$\Delta T_{err}$		d [mm]	<i>h</i> [mm]	$w_b$ [S <sup>-1</sup> ]	$ au_q$ [S]
	$\Delta I_{err}$	Exact	2.00000	0.44000	0.006300	3.00000
Clark	25 mK	Mean value	2.00000	0.43759	0.006321	2.99690
		Deviation	0.00000	0.00281	0.00005	0.03599
		COV [%]	0.00	0.64	0.86	1.20
Ш		Error [%]	0.00	0.63	0.65	0.86
		Mean value	2.00629	0.43971	0.006260	2.96825
	50 ml/	Deviation	0.01089	0.01848	0.000144	0.06273
	50 mK	COV [%]	0.54	4.20	2.30	2.11
		Error [%]	0.31	3.25	1.98	1.86
	A T		7.5	7	- 1-	
	A T		<i>d</i> [mm]	h [mm]	$w_b  [s^{-1}]$	$\tau_q$ [S]
	$\Delta T_{err}$	Exact	2.50000	1.10000	0.006300	$\frac{\tau_q [S]}{3.00000}$
	$\Delta T_{err}$	Exact Mean value				
			2.50000	1.10000	0.006300	3.00000
Clark	$\Delta T_{err}$ 25 mK	Mean value	<b>2.50000</b> 2.50510	<b>1.10000</b> 1.11683	<b>0.006300</b> 0.006204	<b>3.00000</b> 2.98604
Clark IV		Mean value Deviation	2.50000 2.50510 0.01363	1.10000 1.11683 0.01486	0.006300 0.006204 0.00001	3.00000 2.98604 0.01856
		Mean value Deviation COV [%]	2.50000 2.50510 0.01363 0.54	1.10000 1.11683 0.01486 1.33	0.006300 0.006204 0.00001 0.21	3.00000 2.98604 0.01856 0.62
	25 mK	Mean value Deviation COV [%] Error [%]	2.50000 2.50510 0.01363 0.54 0.47	1.10000 1.11683 0.01486 1.33 1.53	0.006300 0.006204 0.00001 0.21 1.52	3.00000 2.98604 0.01856 0.62 0.63
		Mean value Deviation COV [%] Error [%] Mean value	2.50000 2.50510 0.01363 0.54 0.47 2.50793	1.10000 1.11683 0.01486 1.33 1.53 1.08020	0.006300 0.006204 0.00001 0.21 1.52 0.006355	3.00000 2.98604 0.01856 0.62 0.63 3.00681
	25 mK	Mean value Deviation COV [%] Error [%] Mean value Deviation	2.50000 2.50510 0.01363 0.54 0.47 2.50793 0.01973	1.10000 1.11683 0.01486 1.33 1.53 1.08020 0.06984	0.006300 0.006204 0.00001 0.21 1.52 0.006355 0.000308	3.00000 2.98604 0.01856 0.62 0.63 3.00681 0.02167

insight on the accuracy of the inverse solution and its dependency. Table 5 shows the obtained inverse solution for Clark II and Clark IV examples using statistical indicators for noisy measurement data of absolute temperature response, together with the mean error.

As can be seen from Table 5 for Clark II the diameter can be determined very accurately regarding the noise level, while the accuracy of other parameters is in the same range of less than 1 % for low noise level and increases to 2 % to 3% for high noise level. The COV also shows the deviation of the estimated parameters that coinciding with the average error and increases by increasing level of noise, meaning that these parameters will be hard to evaluate in real experimental setup. Similar conclusion can be made for Clark IV example that shows good evaluation of tumor diameter and better evaluation of relaxation time than for Clark II example, while the error for tumor thickness and blood perfusion rate is slightly higher but still in the same range, less than 5 %. This shows that relaxation time can be easily obtained for later stage tumor.

Findings coincide with the findings of our previous work [45], where diameter can be determined very accurately even for the noisy measurement data, regarding the stage of the tumor. And also, that blood perfusion rate and thickness show lower accuracy and interdependence.

Table 6. Solution of the inverse bioheat problem for Clark II and Clark IV example under noisy measurement data sets of temperature difference response;  $F_2(\mathbf{y})$ , showing the mean value, deviation, COV and mean relative error

Clark	A T		d [mm]	h [mm]	$w_b  [s^{-1}]$	$ au_q$ [S]
	$\Delta T_{err}$	Exact	2.00000	0.44000	0.006300	3.00000
		Mean value	2.00045	0.45606	0.006094	2.98212
	OF ml/	Deviation	0.00079	0.01779	0.000302	0.08330
	25 mK	COV [%]	0.04	3.90	4.95	2.79
II		Error [%]	0.02	4.31	4.55	2.16
	50 mK	Mean value	2.02638	0.42853	0.006277	2.93446
		Deviation	0.03468	0.04114	0.000690	0.18607
		COV [%]	1.71	9.60	10.99	6.34
		Error [%]	1.32	6.59	8.54	5.32
	$\Delta T_{err}$		d [mm]	h [mm]	$w_b [s^{-1}]$	$ au_q$ [S]
	$\Delta T_{err}$	Exact	2.50000	1.10000	0.006300	3.00000
	25 mK	Mean value	2.50208	1.07415	0.006387	2.99885
		Deviation	0.00561	0.01426	0.000134	0.01172
Clark		COV [%]	0.22	1.33	2.10	0.39
IV		Error [%]	0.17	2.35	1.79	0.31
		Mean value	2.52163	1.09922	0.006311	3.06237
	50 mK	Deviation	0.03057	0.07763	0.000486	0.06745
	JUIIIN	COV [%]	1.21	7.06	7.70	2.20
		Error [%]	1.15	4.98	5.44	2.42

## 3.3 Type of Thermal Response

Table 6 shows the obtained solution of the inverse problem using temperature difference response for both test examples. Comparing results to the one from Table 5, where absolute temperature response has been used, we can draw the same conclusion of estimating unknown parameters. Accuracy of tumor diameter and relaxation time is still better from the blood perfusion rate and tumor thickness, especially for Clark IV. The relative error of the estimated parameters based on the temperature difference response is higher than the results based on the absolute temperature response, especially for the early-stage tumor. This means it is better to use absolute temperature response to diagnose early-stage tumor. However, using temperature difference response shows that accuracy of the parameters is better for later stage tumor. These findings coincidence with our previous work [45]. Nevertheless, early-stage diagnosis is still possible using temperature difference response and good accuracy of estimated parameters can be obtain by keeping the level of measurement noise low.

From the analysis done on the solution of inverse bioheat problem, we can conclude that all searched parameters can be successfully evaluated even for high level of measurement noise, especially tumor diameter and relaxation time where relative error of the obtained parameters is less than 5 %. Based on this study, it is better to determine unknown parameters using absolute temperature response than temperature difference, especially for an early-stage tumor. However, from the practical point of view, temperature difference response is preferred because it does not depend strongly on the prescribed body core and surrounding temperature, making it more general and still accurate enough.

## 4 CONCLUSIONS

This paper presents a numerical framework for the non-invasive skin cancer diagnosis using dynamic IR thermography, supported by improved skin cancer model and inverse problem analysis, to estimate tumor diameter, thickness, blood perfusion rate and thermal relaxation time. A novel contribution of this work lies in the integration of the non-Fourier DPL bioheat model into a multilayered, axisymmetric skin cancer model, enabling a more realistic simulation of thermal behavior in heterogeneous biological tissues under transient thermal stimuli. The DPL model offers significant advantages over classical Fourier-based models by accounting for thermal lag, finite thermal wave propagation, and directional effects that are critical for capturing fast and localized thermal dynamics near skin tumors. To simulate dynamic thermography response, we used our own developed solver based on subdomain BEM approach that gives accurate solution and proves to be efficient, which is very important for solving inverse bioheat problems.

The inverse bioheat problem solved in this work is to find four important tumor parameters based on the non-Fourier DPL skin cancer model and transient thermal response of dynamic thermography, which also presents the novelty of this work. We analyze two different responses; absolute temperature and temperature difference response on two examples; Clark II and Clark IV stage tumor. Measurement data or thermal response has been generated numerically by prescribing known searched parameters that we would like to retrieve through inverse problem, and direct numerical simulation of dynamic thermography. A measurement noise of 25 mK and 50 mK has been added to the simulated responses for the Clark II and Clark IV tumor, to obtain more realistic measurement data. For dynamic thermography a convective cooling approach with cold air jet has been chosen, which replicates a clinically feasible

dynamic thermography scenario, allowing recording of temperature response during both cooling and rewarming phases. To solve the inverse bioheat problem, a hybrid LM optimization algorithm has been implemented that was combined with direct bioheat problem of simulating dynamic thermography using BEM.

The results showed that solution of the inverse problem does not depend on the initial guess making LM algorithm robust, accurate and efficient for this type of inverse problem. All four parameters can be retrieved exactly only for the measurement data that follows numerical model exactly. However, this is not possible in real life problem. The parameters can be still retrieved very accurately even under higher level of measurement data noise, especially the diameter and thermal relaxation time for both examples using absolute temperature response. Blood perfusion rate and tumor thickness exhibit slightly higher estimation error but remain within acceptable bounds. The accuracy of the estimated parameters is lower when using temperature difference response, however, this is practically more feasible, because the temperature contrast does not depend strongly on the body core temperature or boundary condition at the bottom of the numerical model. For Clark II example, all parameters were estimated with relative errors below 5 % for lower level of measurement noise, demonstrating strong potential for early-stage skin cancer diagnosis.

Overall, this study confirms that dynamic IR thermography, combined with non-Fourier bioheat modeling and inverse analysis, is a promising tool for non-invasive skin cancer assessment. The ability to estimate not only geometric properties but also physiological such as blood perfusion and thermal relaxation time provides insight into tumor size, stage, and invasiveness.

Future work will focus on developing this approach even further in the field of numerical simulations, solving inverse problems, statistical assessment of the approach, as well as on the experimental validation of the proposed model and real-time implementation strategies.

## **References**

- [1] Wilson, A.N., Gupta, K.A., Koduru, B.H., Kumar, A., Jha, A., Cenkeramaddi, L.R. Recent advances in thermal imaging and its applications using machine learning: A review. *IEEE Sens J* 23 3395-3407 (2023) DOI:10.1109/JSEN.2023.3234335.
- [2] Kesztyüs, D., Brucher, S., Wilson, C., Kesztyüs, T. Use of infrared thermography in medical diagnosis, screening, and disease monitoring: A scoping review. Medicina 59 2139 (2023) D0I:10.3390/medicina59122139.
- [3] Manno, M., Yang, B., Bar-Cohen, A. Non-contact method for characterization of small size thermoelectric modules. Rev Sci Instrum 86 084701 (2015) D0I:10.1063/1.4927604.
- [4] Thusyanthan, I., Blower, T., Cleverly, W. Innovative uses of thermal imaging in civil engineering. J Inst Civ Eng 170 1-7 (2016) D01:10.1680/jcien.16.00014.
- [5] Vakrilov, N.V., Kafadarova, N.M., Zlatanski, D.A. Application of infrared imaging in the field of electrical engineering. 2021 XXX International Scientific Conference Electronics (ET) 1-4 (2021) D0I:10.1109/ET52713.2021.9579707.
- [6] Farooq, M., Shariff, W., O'Callaghan, D., Merla, A., Corcoran, P. On the role of thermal imaging in automotive applications: A critical review. *IEEE Access* 11 25152-25173 (2023) DOI:10.1109/ACCESS.2023.3255110.
- [7] Osterman, A., Dular, M., Hocevar, M., Širok, B. Infrared thermography of cavitation thermal effects in water. Stroj Vestn-J Mech E 56 527-534 (2010).
- [8] Lahiri, B., Bagavathiappan, S., Jayakumar, T., Philip, J. Medical applications of infrared thermography: A review. *Infrared Phys Technol* 55 221-235 (2012) D0I:10.1016/j.infrared.2012.03.007.
- [9] Sayasneh, A., Abdelbar, A., Ramajayan, T., Lim, j., Al-karawi, D., Al Zaidi, S., et al. Thermal Camera Application in Gynecological Oncology: Feasibility Study of a Novel Technology. J Oncol Res Ther 9 10203 (2024) D0I:10.29011/2574-710X.10203.
- [10] Ciappara Paniagua, M., Gutierrez Hidalgo, B., Gomez Rivas, J., Redondo Gonzalez, E., De la Parra Sanchez, I., Galindo Herrero, I., et al. Protocol description and initial experience in kidney graft perfusion using infrared thermography, World J Urol 42 416 (2024) D0I:10.1007/s00345-024-05116-9.

- [11] Manullang, M.C.T., Lin, Y.-H., Lai, S.-J., Chou, N.-K. Implementation of Thermal Camera for Non-Contact Physiological Measurement: A Systematic Review. Sensors 21 7777 (2021) D0I:10.3390/s21237777.
- [12] Zhou, Y., Ghassemi, P., Chen, M., McBride, D., Casamento, J.P., Pfefer, T.J., Wang, Q. Clinical evaluation of fever-screening thermography: impact of consensus guidelines and facial measurement location. *J Biomed Opt* 25 097002 (2020) D0I:10.1117/1.JB0.25.9.097002.
- [13] Gorbach, A. M., Heiss, J. D., Kopylev, L., Oldfield, E. H. Intraoperative infrared imaging of brain tumors. J Neurosurg 101 960-969 (2004) DOI:10.3171/ ins.2004.101.6.0960.
- [14] PS, L., M, S., Joy, E. A review on thermography in dentistry. J Evol Med Dent Sci 7 1289-1293 (2018) D0I:10.14260/jemds/2018/294.
- [15] Matos, F., Borba Neves, E., Norte, M., Rosa, C., Machado Reis, V., Vilaça-Alves, J. The use of thermal imaging to monitoring skin temperature during cryotherapy: A systematic review. *Infrared Phys Technol* 73 194-203 (2015) D0I:10.1016/j.infrared.2015.09.013.
- [16] Ammer, K., Ring, E. Application of thermal imaging in forensic medicine. J Imaging Sci 53 125-131 (2005) D0I:10.1179/136821905X50361.
- [17] Bonmarin, M., Le Gal, F. Chapter 31: Thermal imaging in dermatology. Hamblin, M.R., Avci, P., Gupta, G.K. (eds.) Imaging in Dermatology 437-454 (2016) Academic Press, Boston D0I:10.1016/B978-0-12-802838-4.00031-5.
- [18] Godoy, S.E., Hayat, M.M., Ramirez, D.A., Myers, S.A., Padilla, R.S., Krishna, S. Detection theory for accurate and non-invasive skin cancer diagnosis using dynamic thermal imaging. *Biomed. Opt Express* 8 2301-2323 (2017) D0I:10.1364/B0E.8.002301.
- [19] Strąkowska, M., Strąkowski, R., Strzelecki, M., De Mey, G., Więcek, B. Evaluation of perfusion and thermal parameters of skin tissue using cold provocation and thermographic measurements. *Metrol Meas Syst* 23 373-381 (2016) D0I:10.1515/mms-2016-0032.
- [20] Strąkowska, M., Strąkowski, R., Strzelecki, M., De Mey, G., Więcek, B. Thermal modelling and screening method for skin pathologies using active thermography. *Biocybern Biomed Eng* 38 602-610 (2018) D0I:10.1016/j.bbe.2018.03.009.
- [21] Elder, D. E. Tumor progression, early diagnosis and prognosis of melanoma. Acta Oncol 385 535-548 (1999) D01:10.1080/028418699431113.
- [22] Flores-Sahagun, J., Vargas, J., Brenner, F. Analysis and diagnosis of basal cell carcinoma (BCC) via infrared imaging. *Infrared Phys Technol* 54 367-378 (2011) D0I:10.1016/j.infrared.2011.05.002.
- [23] Smith, R.L., Soeters, M.R., Wüst, R.C.I., Houtkooper, R.H. Metabolic flexibility as an adaptation to energy resources and requirements in health and disease. *Endocr Rev* 39 489-517 (2018) D0I:10.1210/er.2017-00211.
- [24] Santulli, G., Angiogenesis. Insights from a Systematic Overview. (2013) Nova Publisher, Hauppauge.
- [25] Jiang, L.J., Ng, E.Y.K., Yeo, A.C.B., Wu, S., Pan, F., Yau, W.Y., Yang, Y. A perspective on medical infrared imaging. J Medical Eng Technol 29 257-267 (2005) D0I:10. 1080/03091900512331333158.
- [26] Clark, W.H.Jr., From, L., Bernardino, E.A., Mihm, M.C. The histogenesis and biologic behavior of primary human malignant melanomas of the skin. Cancer Res 29 705 (1969).
- [27] Breslow, A. Thickness, cross-sectional areas and depth of invasion in the prognosis of cutaneous melanoma. Ann Surg 172 902-908 (1970) DOI:10.1097/00000658-197011000-00017.
- [28] Duarte, A.F., Sousa-Pinto, B., Azevedo, L.F., Barros, A.M., Puig, S., Malvehy, J., Haneje, E., Correia, O. Clinical ABCDE rule for early melanoma detection. Eur J Dermatol 31 771-778 (2021) D0I:10.1684/ejd.2021.4171.
- [29] Herman, C. The role of dynamic infrared imaging in melanoma diagnosis. Expert Rev Dermatol 8 177-184 (2013) D0I:10.1586/edm.13.15.
- [30] Wilson, J.B. Excisional Biopsy of Dermal and Subcutaneous Lesions. Chen, H. (ed.), Illustrative Handbook of General Surgery. (2016) 781-791 Springer International Publishing, Cham D0I:10.1007/978-3-319-24557-7\_44.
- [31] Verstockt, J., Verspeek, S., Thiessen, F., Tjalma, W.A., Brochez, L., Steenackers, G. Skin cancer detection using infrared thermography: Measurement setup, procedure and equipment. Sensors 22 3327 (2022) D0I:10.3390/s22093327.
- [32] Saxena, A., Ng, E., Lim, S.T. Active dynamic thermography to detect the presence of stenosis in the carotid artery. Comput Biol Med 120 103718 (2020) D0I:10.1016/j.compbiomed.2020.103718.
- [33] Çetingül, M.P., Herman, C. Quantification of the thermal signature of a melanoma lesion. Int J Therm Sci 50 421-431 (2011) D0I:10.1016/j. ijthermalsci.2010.10.019.
- [34] Jiang, L., Zhan, W., Loew, M.H. Modeling static and dynamic thermography of the human breast under elastic deformation. *Phys Med Biol* 56 187-202 (2010) D0I:10.1088/0031-9155/56/1/012.
- [35] Vardasca, R., Vaz, L., Mendes, J. Classification and decision making of medical

- infrared thermal images. Dey, N., Ashour, A., Borra, S. (eds.) *Classification in BioApps* 79-104 (2018) Springer, Cham **D0I:10.1007/978-3-319-65981-7\_4**.
- [36] Kirimtat, A., Krejcar, O., Selamat, A. A mini-review of biomedical infrared thermography (B-IRT). Bioinformatics and Biomedical Engineering - IWBBIO (2019) 99-110 D0I:10.1007/978-3-030-17935-9\_10.
- [37] Ammer, K., Ring, E. Standard procedures for infrared imaging in medicine, Bronzino, J.D. (ed.) Medical Devices and Systems (2012) 1-14 CRC Press, Taylor & Francis Group.
- [38] Ring, E.F., Jones, C., Ammer, K., Plassmann, P., Bola, T.S. Cooling effects of deep freeze cold gel compared to that of an ice pack applied to the skin. *Thermol Int* 14 93-98 (2004).
- [39] Carlo, A.D. Thermography and the possibilities for its applications in clinical and experimental dermatology. Clin Dermatol 13 329-36 (1995) D0I:10.1016/0738-081x(95)00073-0.
- [40] Magalhaes, C., Vardasca, R., Rebelo, M., Valenca-Filipe, R., Ribeiro, M., Mendes, J. Distinguishing melanocytic nevi from melanomas using static and dynamic infrared thermal imaging. J Eura cad Dermatol Venereol 33 1700-1705 (2019) D0I:10.1111/jdv.15611.
- [41] Çetingül, M., Alani, R., Herman, C., Quantitative evaluation of skin lesions using transient thermal imaging. Proceedings of the 14<sup>th</sup> International Heat Transfer Conference 31-39 (2010) D0I:10.1115/IHTC14-22465.
- [42] Bhowmik, A., Repaka, R. Estimation of growth features and thermophysical properties of melanoma within 3-D human skin using genetic algorithm and simulated annealing. Int J Heat Mass Transf 98 81-95 (2016) D0I:10.1016/j. ijheatmasstransfer.2016.03.020.
- [43] Cheng, T.-Y., Herman, C. Analysis of skin cooling for quantitative dynamic infrared imaging of near-surface lesions. *Int J Therm Sci* 86 175-188 (2014) D0I:10.1016/j.ijthermalsci.2014.06.033.
- [44] Çetingül, M. P., Herman, C., A heat transfer model of skin tissue for the detection of lesions: sensitivity analysis. Phys Med Biol 55 5933-5951 (2010) D0I:10.1088/0031-9155/55/19/020.
- [45] Iljaž, J., Wrobel, L.C., Gomboc, T., Hriberšek, M., Marn, J. Solving inverse bioheat problems of skin tumour identification by dynamic thermography. *Inverse Probl* 36 035002 (2020) D0I:10.1088/1361-6420/ab2923.
- [46] Luna, J. M., Guerrero, A.H., Méndez, R.R., Ortiz, J.L.L. Solution of the inverse bioheat transfer problem for a simplified dermatological application: Case of skin cancer. *Ing Mec Tecnol Desarro* 4 219-228 (2014).
- [47] Partridge, P.W., Wrobel, L.C. A coupled dual reciprocity BEM/genetic algorithm for identification of blood perfusion parameters. *Int J Numer Methods Heat Fluid Flow* 19 25-28 (2009) **D0I:10.1108/09615530910922134**.
- [48] Partridge, P.W., Wrobel, L.C. An inverse geometry problem for the localisation of skin tumours by thermal analysis. *Eng Anal Bound Elem* 31 803-811 (2007) D0I:10.1016/j.enganabound.2007.02.002.
- [49] Fu, Z.-J., Chu, W.-H., Yang, M., Li, P.-W., Fan, C.-M. Estimation of tumor characteristics in a skin tissue by a meshless collocation solver. *Int J Comput Methods* 18 2041009 (2021) D0I:10.1142/S0219876220410091.
- [50] Bhowmik, A., Repaka, R., Mishra, S.C. Thermographic evaluation of early melanoma within the vascularized skin using combined non-Newtonian blood flow and bioheat models. Comput Biol Med 53 206-219 (2014) D0I:10.1016/j. compbiomed.2014.08.002.
- [51] Bonmarin, M., Le Gal, F.-A. Lock-in thermal imaging for the early-stage detection of cutaneous melanoma: a feasibility study. Comput Biol Med 47 36-43 (2014) D0I:10.1016/j.compbiomed.2014.01.008.
- [52] Iljaž, J., Wrobel, L.C., Hriberšek, M., Marn, J. The use of design of experiments for steady-state and transient inverse melanoma detection problems. Int J Therm Sci 135 256-275 (2019) D0I:10.1016/j.ijthermalsci.2018.09.003.
- [53] Iljaž, J., Wrobel, L.C., Hriberšek, M., Marn, J. Numerical modelling of skin tumour tissue with temperature-dependent properties for dynamic thermography. Comput Biol Med 112 103367 (2019) D0I:10.1016/j.compbiomed.2019.103367.
- [54] Tucci, C., Trujillo, M., Berjano, E., Iasiello, M., Andreozzi, A., Vanoli, G.P. Pennes' bioheat equation vs. porous media approach in computer modeling of radiofrequency tumor ablation. Sci Rep 11 5272 (2021) D0I:10.1038/s41598-021-84546-6.
- [55] Kabiri, A., Talaee, M.R. Analysis of hyperbolic Pennes bioheat equation in perfused homogeneous biological tissue subject to the instantaneous moving heat source. SN Appl Sci 3 398 (2021) D0I:10.1007/s42452-021-04379-w.
- [56] Verma, R. Kumar, S. Computational study on 2D three-phase lag bioheat model during cryosurgery using RBF meshfree method. J Therm Biol 114 103575 (2023) D0I:10.1016/j.jtherbio.2023.103575.
- [57] Kang, Z., Zhu, P., Gui, D., Wang, L. A method for predicting thermal waves in dual-phase-lag heat conduction. Int J Heat Mass Transf 115 250-257 (2017) D0I:10.1016/j.ijheatmasstransfer.2017.07.036.

- [58] Ma, J., Yang, X., Sun, Y., Yang, J. Thermal damage in three-dimensional vivo biotissues induced by moving heat sources in laser therapy. Sci Rep 9 10987 (2019) D0I:10.1038/s41598-019-47435-7.
- [59] Namakshenas, P., Mojra, A. Microstructure-based non-Fourier heat transfer modeling of HIFU treatment for thyroid cancer. Comput Methods Programs Biomed 197 105698 (2020) D0I:10.1016/j.cmpb.2020.105698.
- [60] Tzou, D.Y. Thermal shock waves induced by a moving crack a heat flux formulation. Int J Heat Mass Transf 33 877-885 (1990) DOI:10.1016/0017-9310(90)90071-2.
- [61] Tzou, D. Macro- To Micro-Scale Heat Transfer: The Lagging Behavior. (2014) Taylor & Francis, Chichester D0I:10.1002/9781118818275.
- [62] Stryczyński, M., Majchrzak, E. Numerical modelling of the laser high-temperature hyperthermia using the dual-phase lag equation. J Theor Appl Mech 62 389-401 (2024) D0I:10.15632/jtam-pl/186178.
- [63] Singh, S., Bianchi, L., Korganbayev, S., Namakshenas, P., Melnik, R., Saccomandi, P. Non-Fourier bioheat transfer analysis in brain tissue during interstitial laser ablation: Analysis of multiple influential factors. Ann Biomed Eng 52 967-981 (2024) D0I:10.1007/s10439-023-03433-5.
- [64] Verma, R., Kalita, J.C. Numerical simulation of phase change dual-phase-lag bioheat model with nanocryosurgery using radial basis function meshfree approach. J Heat Transf 147 061201 (2025) D0I:10.1115/1.4067611.
- [65] Liu, K.-C., Chen, H.-T. Investigation for the dual phase lag behavior of bio-heat transfer. Int J Therm Sci 49 1138-1146 (2010) DOI:10.1016/j. ijthermalsci.2010.02.007.
- [66] Yong, Z., Chen, B., Li, D. Non-Fourier effect of laser-mediated thermal behaviors in bio-tissues: A numerical study by the dual-phase-lag model. *Int J Heat Mass Transf* 108 1428-1438 (2017) D0I:10.1016/j.ijheatmasstransfer.2017.01.010.
- [67] Kishore, P., Kumar, S. Thermal relaxation parameters estimation of non-Fourier heat transfer in laser-irradiated living tissue using the Levenberg-Marquardt algorithm. Numer Heat Transf A-Appl 1-26 (2024) D0I:10.1080/10407782.2024 .2314232.
- [68] Horvat, I.D., Iljaž, J. Numerical modeling of non-Fourier bioheat transfer in multilayer biological tissue using BEM to simulate dynamic thermography in skin tumor diagnostics. Eng Anal Bound Elem 179 106408 (2025) D0I:10.1016/j. enganabound.2025.106408.
- [69] Cruz, G. A.S., Bertotti, J., Dynamic infrared imaging of cutaneous melanoma and normal skin in patients treated with BNCT. Appl Radiat Isot 67 54-58 (2009) D0I:10.1016/j.apradiso.2009.03.093.
- [70] Gomboc, T., Iljaž, J., Wrobel, L.C., Hriberšek, M., Marn, J. Design of constant temperature cooling device for melanoma screening by dynamic thermography. Eng Anal Bound Elem 125 66-79 (2021) D0I:10.1016/j. enganabound.2021.01.009.
- [71] Liu, K.-C., Wang, Y.-N., Chen, Y.-S. Investigation on the bio-heat transfer with the dual-phase-lag effect. Int J Therm Sci 58 29-35 (2012) D0I:10.1016/j. iithermalsci.2012.02.026.
- [72] Pennes, H.H. Analysis of tissue and arterial blood temperatures in the resting human forearm. J Appl Physiol 85 93-122 (1948) D0I:10.1152/jappl.1998.85.1.5.
- [73] Godoy, S.E., Ramirez, D.A., Myers, S.A., Winckel, G., Krishna, S., Berwick, M., et al. Dynamic infrared imaging for skin cancer screening. *Infrared Phys Technol* 70 147-152 (2015) D0I:10.1016/j.infrared.2014.09.017.
- [74] Antaki, P.J. New Interpretation of Non-Fourier Heat Conduction in Processed Meat. *J Heat Transf* 127 189-193 (2005) **D0I:10.1115/1.1844540**.
- [75] Mabeta, P. Paradigms of vascularization in melanoma: Clinical significance and potential for therapeutic targeting. *Biomed Pharmacother* 127 110135 (2020) D0I:10.1016/j.biopha.2020.110135.
- [76] Quintanilla, R., Racke, R. A note on stability in dual-phase-lag heat conduction. Int J Heat Mass Transf 49 1209-1213 (2006) D0I:10.1016/j. ijheatmasstransfer.2005.10.016.
- [77] Majchrzak, E., Kałuża, G., Poteralska, J. Application of the DRBEM for numerical solution of Cattaneo-Vernotte bioheat transfer equation. Sci Res Inst Math Comput Sci 7 111-120 (2008).
- [78] Ciesielski, M., Duda, M., Mochnacki, B. Comparison of bio-heat transfer numerical models based on the Pennes and Cattaneo-Vernotte equations. J Appl Math Comput Mech 15 33-38 (2016) D0I:10.17512/jamcm.2016.4.04.
- [79] Liu, K.-C., Wang, Y.-N., Chen, Y.-S. Investigation on the bio-heat transfer with the dual-phase-lag effect. Int J Therm Sci 58 29-35 (2012) D0I:10.1016/j. iithermalsci.2012.02.026.
- [80] Felde, I., Réti, T. Evaluation of hardening performance of cooling media by using inverse heat conduction methods and property prediction. Stroj Vestn-J Mech E 56 77-83 (2010).

- [81] Roy, A.D., Dhiman, S.K. Estimation of surface temperature and heat flux over a hollow cylinder and slab using an inverse heat conduction approach. Stroj Vestn-J Mech E 70 342-354 (2024) D0I:10.5545/sv-jme.2023.864.
- [82] Nguyen, T.-T., Le, M.-T. Optimization of the internal roller burnishing process for energy reduction and surface properties. Stroj Vestn-J Mech E 67 167-179 (2021) D0I:10.5545/sv-jme.2021.7106.
- [83] Afsharzadeh, N., Yazdi, M.E., Lavasani, A.M. Thermal design and constrained optimization of a fin and tube heat exchanger using differential evolution algorithm. Stroj Vestn-J Mech E 71 10-20 (2025) D0I:10.5545/sv-jme.2023.887.
- [84] Mei, J., Xie, S., Liu, H., Zang, J. Hysteresis modelling and compensation of pneumatic artificial muscles using the generalized Prandtl-Ishlinskii model. Stroj Vestn-J Mech E 63 657-665 (2017) DOI:10.5545/sv-jme.2017.4491.

**Acknowledgements** The authors thank the Slovenian Research and Innovation Agency (ARIS) for the research core funding No. P2-0196 and No. J7-60118.

Received 2025-04-25, revised 2025-09-01, accepted 2025-09-11 as Original scientific paper 1.01.

**Data availability** The data that supports the findings of this study are available from the corresponding author upon reasonable request.

**Author contribution** Ivan Dominik Horvat: Data curation, Formal analysis, Investigation, Methodology, Software, Validation and Writing – review & editing; and Jurij Iljaž: Conceptualization, Formal analysis, Supervision, Visualization and Writing – original draft.

# Numerično reševanje inverznega problema dinamične termografije za diagnostiko kožnega raka na osnovi nefourierovega modela prenosa toplote

Povzetek Članek obravnava numerično reševanje inverznega problema prenosa toplote za določitev štirih parametrov kožnega raka: premer, debelino, perfuzijski pretok krvi in relaksacijski čas. Določitev temelji na toplotnem odzivu kože pridobljenim z dinamično termografijo ter numeričnim modelom kožnega raka ki lahko bistveno izboljša diagnostično vrednost termografije. Za čim bolj realističen opis prenosa toplote v tkivu med procesom dinamične termografije je bil uporabljen nefourierov model z dvojnim faznim zamikom. Model kožnega raka je sestavljen iz večplastne kože, podkožne maščobe in mišice ter kožnega raka oziroma tumorja. Za rešitev kompleksnega nefourierovega modela ter simulacije dinamične termografije je bil razvit programski paket na osnovi metode robnih elementov. Simulacija dinamične termografije, ki za temperaturno vzbujanje uporablja curek hladnega zraka, je pomembna za rešitev inverznega problema, saj z njo pridemo do termičnega odziva oziroma temperaturnega kontrasta na površini kože pri predpostavljenih iskanih parametrih ter njene primerjave z meritvijo. Tako je bil inverzni problem rešen s pristopom optimizacije, pri čemer je bil uporabljen Levenberg-Marquardt algoritem. Meritve so bili pri tem generirane numerično z vnaprej znanimi parametri tumorja in dodanim šumom za ovrednotenje natančnost in občutlijvost inverzne rešitve. Rešitev inverznega problema je bila pri tem testirana za dva različna temperaturna odziva, in sicer absolutno temperaturo in temperaturno razliko, kakor tudi za dve različni stadija tumorja kot je Clark II, ki predstavlja zgodnji stadij in Clark IV, ki predstavlja pozni stadij. Vsi pomembni parametri tumorja so bili uspešno določeni tudi pri visoki stopnji šuma, zlasti premer in relaksacijski čas, pri čemer je bila natančnost ovrednotenih parametrov nekoliko boljša z uporabo absolutnega temperaturnega odziva. Rezultati kažejo na robustno in obetavno metodo za zgodnjo diagnostiko kožnega raka in pomembno prispevajo na področju modeliranja prenosa toplote v bioloških tkivih, reševanju inverznih problemov ter razvoju dinamične termografije.

**Ključne besede** numerično reševanje, dinamična termografija, inverzni problem, nefourierov prenos toplote, DPL model, metoda robnih elementov, Levenberg-Marquardt optimizacija